Identification of the central compact object in the young supernova remnant 1E 0102.2-7219

Frédéric P.A. Vogt[1,2][*], Elizabeth S. Bartlett[1,2], Ivo R. Seitenzahl[3,4], Michael A. Dopita[4],
Parviz Ghavamian[5], Ashley J. Ruiter[4,6,3], Jason P. Terry[7]

[1]European Southern Observatory, Av. Alonso de Córdova 3107, 763 0355 Vitacura, Santiago, Chile

[2]ESO Fellow

[3]School of Physical, Environmental and Mathematical Sciences, University of New South Wales,
Australian Defence Force Academy, Canberra, ACT 2600, Australia

[4]Research School of Astronomy and Astrophysics, Australian National University, Canberra, ACT 2611, Australia

[5]Department of Physics, Astronomy and Geosciences, Towson University, Towson, MD, 21252, USA

[6]ARC Centre for All-sky Astrophysics (CAASTRO).

[7]Department of Physics and Astronomy, University of Georgia, Athens, GA, USA

Accepted for publication in Nature Astronomy

Disclaimer

What follows is the article as originally submitted to Nature Astronomy. This article has been accepted for publication after 2 rounds of reviews on 28 February 2018. As per Nature Astronomy's publication policies, we must delay for 6 months the upload of the accepted article to the arXiv. In addition to minor changes, the major modifications to this article following the review process (not included in the present version) are:

- *the explicit dismissal of alternative scenarios for the X-ray point source (incl. a High Mass X-ray Binary, an X-ray bright foreground star, a Low Mass X-ray Binary, a white dwarf, or a Super Soft X-ray Source) based on both the optical upper limits for the optical counterpart derived from HST and statistical arguments,*

- *a "goodness-of-fit" analysis of the X-ray source using power laws, demonstrating that the X-ray energy distribution of the source is incompatible with that of a pulsar wind nebula, and*

- *the derivation of a black-body radius of $8.7^{+4.9}_{-2.7}$ km for the neutron star.*

Until its inevitable upload to the arXiv, readers interested in the latest version of this article are encouraged to contact F.P.A. Vogt directly.

---

[*]frederic.vogt@alumni.anu.edu.au

Oxygen-rich (O-rich) young supernova remnants (SNRs) are valuable objects for probing the outcome of nucleosynthetic processes in massive stars, as well as the physics of supernova explosions. Observed a few thousand years after the supernova explosion, the known O-rich SNRs are Puppis A, Cas A, and G292.2+1.8 in our Galaxy, 0540-69.3, N132D, and 1E 0102.2-7219 (E 0102 for short) in the Magellanic Clouds, and a young remnant in NGC 4449. These systems contain fast-moving oxygen-rich and hydrogen-poor filaments visible at optical wavelengths: fragments of the progenitor's stellar interior expelled at a few 1000 km s^{-1} during the supernova explosion. Here we report for the first time the identification of the compact object in E 0102 in reprocessed *Chandra X-ray Observatory* (*CXO*) data, enabled via the discovery of ring-shaped emission from warm ionized oxygen-rich and neon-rich material at optical wavelengths. The optical ring, discovered in integral field spectroscopy observations from the Multi Unit Spectroscopic Explorer (MUSE) at the Very Large Telescope, has a radius of $(2.10 \pm 0.35)\,''{\equiv}(0.63 \pm 0.11)$ pc, and a width of $(1.80 \pm 0.35)\,''{\equiv}(0.54 \pm 0.11)$ pc. It surrounds an X-ray point source with an intrinsic 1.2–2.0 keV X-ray luminosity L_i (1.2–2.0 keV)$= (1.4 \pm 0.2) \times 10^{33}$ erg s^{-1}. This luminosity, its energy distribution consistent with a soft thermal-like spectrum, together with the lack of any optical counterpart in existing archival observations from the *Hubble Space Telescope* (*HST*), indicates that this object is an isolated neutron star: a Central Compact Object akin to those present in the Cas A and Puppis A SNRs.

E 0102 is located in the Small Magellanic Cloud, at a distance of 62 kpc (Graczyk et al. 2014; Scowcroft et al. 2016). It was first identified as an O-rich SNR using optical narrow-band imaging (Dopita et al. 1981), on the basis of its initial X-ray detection by the Einstein Observatory (Seward & Mitchell 1981). The measurement of the O-rich ejecta's proper motions, using *HST* observations spanning an 8-year baseline, indicate an age of 2050±600 yr (Finkelstein et al. 2006). The paucity of emission from oxygen-burning products (S, Ca, Ar) originally suggested a Type Ib progenitor (Blair et al. 2000), but the recent detection of [S II] $\lambda\lambda6716,6731$ and Hα emission in localized, fast, knots calls this into question (Seitenzahl et al. 2018). In October 2016, we obtained new observations of E 0102 with the MUSE optical integral field spectrograph (Bacon et al. 2010) mounted on the Nasmyth B of the Unit Telescope 4 of ESO's Very Large Telescope at the observatory of Cerro Paranal in Chile, under Director Discretionary Time program 297.D-5058 (P.I.: Vogt). This dataset (see the Supplementary Material for details on the observations and data processing), covers the entire spatial extent of the remnant (see Fig. 1) with a seeing limited resolution of $0.7''{\equiv}0.21$ pc and a spectral range of $4750{\rightarrow}9350$ Å. The spatio-kinematic complexity of the supernova ejecta is revealed in the MUSE data primarily in the light of [O III] $\lambda\lambda4959,5007$. In the coronal lines of [Fe XIV] $\lambda5303$, [Fe XI] $\lambda7892$ and [Fe X] $\lambda6375$, this MUSE dataset also revealed for the first time a thin shell (in emission) surrounding the fast ejecta, tracing the impact of the forward shock wave at optical wavelengths (Vogt et al. 2017).

In this Report, we present the discovery of a new structure in E 0102 revealed by our MUSE observations; a pc-scale low-ionization "optical ring" visible (in emission) in 32 recombination lines of O I and Ne I (see Fig. 1), as well as [C I] $\lambda8727$, [O I] $\lambda6300$, and [O I] $\lambda6364$. A coincident but spatially more extended high-ionization ring-like structure is visible in the forbidden lines of [O III] and [O II]. The low-ionization ring –the detailed spectral characterization of which is included in the Supplementary Material– lacks optical emission from hydrogen and helium, indicating that it is largely composed of heavy elements. Yet, its spectral signature differs from that of the typical fast ejecta in the system. Optical recombination lines such as Ne I $\lambda6402$, O I $\lambda7774$ and O I $\lambda8446$ dominate over forbidden emission lines, which suggests a low temperature and high density for this structure. This is indicative of different physical conditions *in situ* and/or a different excitation mechanism from that of the O-rich fast ejecta encountering the reverse shock (Sutherland & Dopita 1995). The median line-of-sight (LOS) velocity of the optical ring is redshifted by (55 ± 10) km s^{-1} with respect to the SMC rest-frame (measured in the MUSE datacube using the background H II-region-like emission as velocity reference).

The existence of an X-ray point source in the middle of the low-ionization optical ring yields important clues regarding the exact nature of this structure. We identified this X-ray point source after reprocessing 322.6 ks of *CXO* observations of E 0102 (see Fig. 1). With an X-ray flux of $F(0.5$–7.0 keV$)=(1.4 \pm 0.2) \times 10^{-14}$ erg cm^{-2} s^{-1} (see the Supplementary Material for details), the X-ray point source is located at:

$$\text{R.A: } 01^h04^m02.7^s \text{ — Dec: -72}°02'00.2'' \text{ [J2000].} \quad (1)$$

The estimated absolute uncertainty of this position is $1.2''$, stemming both from the accuracy of the World Coordinate System (WCS) solution of the combined *CXO* observations, and the complex X-ray background of E 0102. One can expect ~70 X-ray sources with $F(0.5$–2.0 keV$)>1.0 \times 10^{-14}$ erg cm^{-2} s^{-1} per degree square (Gilli et al. 2007). Given that the area of the elliptical structure seen by MUSE is ~15 square arcsec, the probability of this X-ray source to lie in the background (i.e. a *chance alignment*) is extremely low, with only 8×10^{-5} similar (or brighter) background sources expected for this area. The spatial coincidence of the optical ring and the X-ray point source is
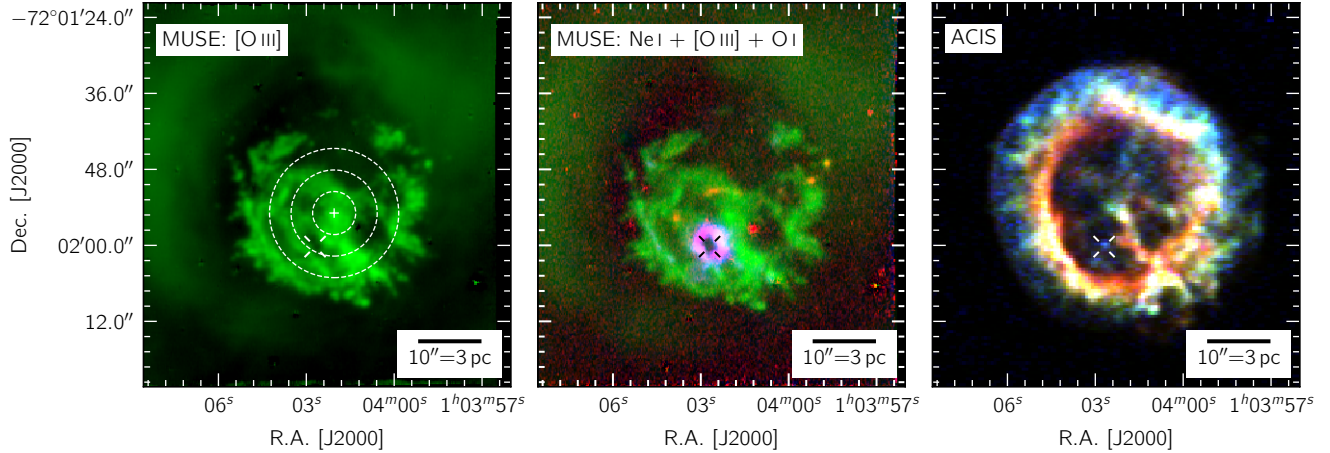
Figure 1: **Global optical and X-ray view of E 0102.** Left: continuum-subtracted MUSE view of E 0102 in the light of [O III] $\lambda\lambda4959,5007$, showing the complex structure of the fast ejecta in this system. The proper motion center of the fast ejecta and its associated 1-σ, 2-σ, and 3-σ uncertainty areas derived from *HST* observations (Finkelstein et al. 2006) is shown using a white "+" and concentric dashed circles. Middle: continuum-subtracted MUSE view of E 0102 in the light of Ne I $\lambda6402$ (red channel; 80 km s^{-1} velocity range), [O III] $\lambda\lambda4959,5007$ (green channel; full velocity range) and O I $\lambda7774$ (blue channel; 80 km s^{-1} velocity range). A ring-like structure with a distinct spectral signature is visible in light pink. Right: Chandra ACIS pseudo-RGB image of E 0102 (red channel: 0.5-1.2 keV, green channel: 1.2-2.0 keV, blue channel: 2.0-7.0 keV), with a (native ACIS) pixel scale of 0.492$''$. A crosshair marker indicates the location of the X-ray point source *p1* in all panels.

thus a strong indication that the X-ray point source is located in the SMC, and directly associated with the elliptical structure itself.

An earlier, dedicated search for a compact object in E 0102 (Rutkowski et al. 2010) already located the same X-ray point source described above[1]. For consistency, we shall thus adopt here the same name for it: "*p1*". This source was then merely listed as one candidate among seven sources within E 0102, but with no explicit comment. We hypothesize that source *p1* may have (then) escaped a definitive identification in part due to its embedment in the diffuse and confusing background X-ray emission interior to E 0102. Today, it is the unique capabilities of MUSE (i.e. its high sensitivity, fine spatial sampling and R≅3000 spectral resolution) that make it possible to spatio-kinematically isolate a distinctive optical ring of ejecta material centered on the X-ray source, thereby allowing us to firmly associate *p1* with the SNR.

Evidently, the existence of an X-ray point source physically associated with E 0102 begs the question: could *p1* be the as-of-yet unidentified compact object leftover by the supernova? In the other O-rich SNRs, compact objects come in two distinct types: (a) pulsars with active pulsar wind nebulae, as detected in G292.0+1.8 (Camilo et al. 2002; Park et al. 2007) and 0540-69.3 (Seward et al. 1984; Middleditch & Pennypacker 1985; Mignani et al. 2010), and (b) Central Compact Objects (CCOs), as detected in Puppis

A (Petre et al. 1996) and Cas A (Chakrabarty et al. 2001; Mereghetti et al. 2002). CCOs lack evidence of a pulsar wind nebula. They are detected only via their blackbody radiation, and are understood to be isolated, cooling neutron stars with thermal X-ray luminosities $L \cong 10^{33.5}$ erg s^{-1} (Viganò et al. 2013). Extensive optical searches have failed to find any counterparts to the CCOs in Cas A and Puppis A, setting strong constraints on the possible accretion rate of material from the immediate surroundings of these objects (Wang et al. 2007; Mignani et al. 2009).

The low counts associated with the *CXO* observations of the source *p1* hinder our ability to perform a detailed "direct" spectral analysis. Instead, for comparison purposes, we first simulate how the CCO of Cas A, whose X-ray signature has been extensively modelled (Pavlov & Luna 2009), would appear if it were located at the distance of the SMC. We also fit a series of absorbed, single blackbody models to the energy distribution of the source *p1*. Both the Cas A-like CCO spectra at the distance of the SMC and our best-fit, single blackbody model with $kT_{BB} = 0.19$ keV are compared to the energy distribution of *p1* in Fig. 2. From our modelling, we derive an intrinsic (unabsorbed) luminosity of the source *p1* of L_i (1.2–2.0 keV)= $(1.4 \pm 0.2) \times 10^{33}$ erg s^{-1}. Although the Cas A-like CCO spectrum is hotter than that of the source *p1*, the overall brightness of both sources are comparable. A detailed description of our simulations is included in the Supplementary Material.

We searched for an optical counterpart to *p1* in archival images from the Wide-Field Camera 3 (WFC3) and Ad-

---

[1] Although Rutkowski et al. (2010) never explicitly quote the coordinate of *p1*, its location is made clear from their Fig. 1.
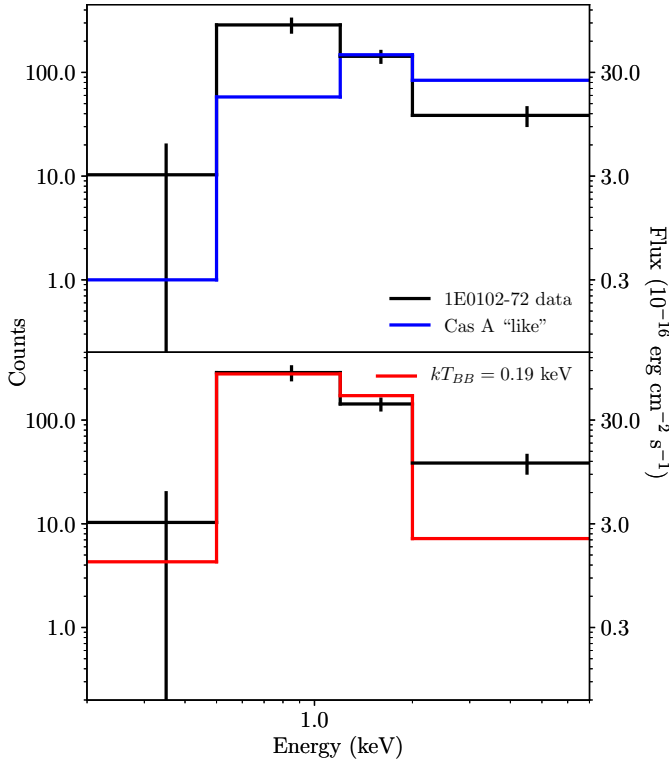
Figure 2: **X-ray spectral signature of *p1*, and associated modelling**. Energy distribution of the X-ray point source *p1* in E 0102 (black curve), compared with that of a Cas A-like CCO observed at the same distance (blue curve, top), and our best-fit, absorbed, single blackbody component model with $kT_{BB} = 0.19$ keV (red curve, bottom). Given its brightness and spectral signature, *p1* is consistent with being a CCO, ~ 0.2 keV cooler than that of Cas A (Pavlov & Luna 2009).

vanced Camera for Survey (ACS) on the *HST*. We found no suitable candidate down to an apparent magnitude upper limit of $m_{\mathrm{F775W}} > 24.5$ (see the Supplementary Material for details). Altogether, these observational characteristics (X-ray brightness, X-ray energy distribution consistent with a soft thermal-like spectrum, lack of an optical counterpart and pulsar wind nebula, and spatial location; Pavlov et al. 2004) lead us to propose the X-ray source *p1* as a new addition to the CCO family, and the first identified extragalactic CCO.

We now focus on the nature of the optical ring surrounding this CCO. The elliptical structure has a semi-major axis of $(2.10 \pm 0.35)\,''{\equiv}(0.63 \pm 0.11)\,$pc, an ellipticity $b/a = (1.20 \pm 0.05)^{-1}$, and a ring-width of $(1.80 \pm 0.35)\,''{\equiv}(0.54 \pm 0.11)\,$pc (see Fig. 3). We find evidence of (at least) four intensity discontinuities along the ring to the N, S, E and S-W (see Fig. 4). Unambiguously identifying sub-structures within the ring itself will require sharper follow-up observations. In the *HST* WFC3 F502N image presented in Fig. 3, we note that a thin elliptical arc is present near the inner edge of the area coincident with the optical ring seen by MUSE, with a semi-major axis of $(1.65 \pm 0.04)\,''{\equiv}(0.50 \pm 0.01)\,$pc. Given the spectral transmission window of the F502N filter, this arc is most certainly detected via its [O III] $\lambda\lambda 4959, 5007$ emission. However, unambiguously separating it from the complex structure of the O-rich fast ejecta in this area is not straightforward. In the light of [O III] $\lambda\lambda 4959, 5007$, our MUSE observations suggest that the high-ionization ring may be connected to a larger, funnel-like structure of shocked ejecta oriented along the line of sight.

We performed a full spectral fit of the low-ionization optical ring (on a spaxel-by-spaxel basis, see the Supplementary Material for details), and derived its line-of-sight (LOS) kinematics (presented in Fig. 4). We find a clear asymmetry of $\Delta v_{\mathrm{los}} = (100 \pm 21)$ km s^{-1} for the gas LOS velocity, broadly aligned with the ring's major axis rotated by $(20 \pm 5)°$ East-of-North. The distance from the low-ionization ring to the CCO implies an escape velocity of $\lesssim 1$ km s^{-1}: given its LOS velocity, the ring material is thus not gravitationally bound to the CCO. Despite an evident *blueshifted trough* to the West (possibly due to intervening fast ejecta in the line of sight biasing the measurements of the line kinematics), the overall pattern is suggestive of an expanding torus, tilted with respect to the plane-of-the-sky, by $33°.5^{+3.5}_{-4.5}$, with an absolute expansion velocity of 90.5^{+40}_{-30} km s^{-1}. If the torus has been expanding ballistically, this would imply an age of 6800^{+5400}_{-2900} yr for the structure. This age is somewhat older than (though not incompatible with) the supernova age derived from the proper motion of the O-bright fast ejecta (Finkelstein et al. 2006), given the associated uncertainties. We discourage any over-interpretation of the arcsec-scale structures of the ring velocity map, recalling both the limited spatial resolution of the observations, and the existence of typical kinematic fitting artefacts asso-
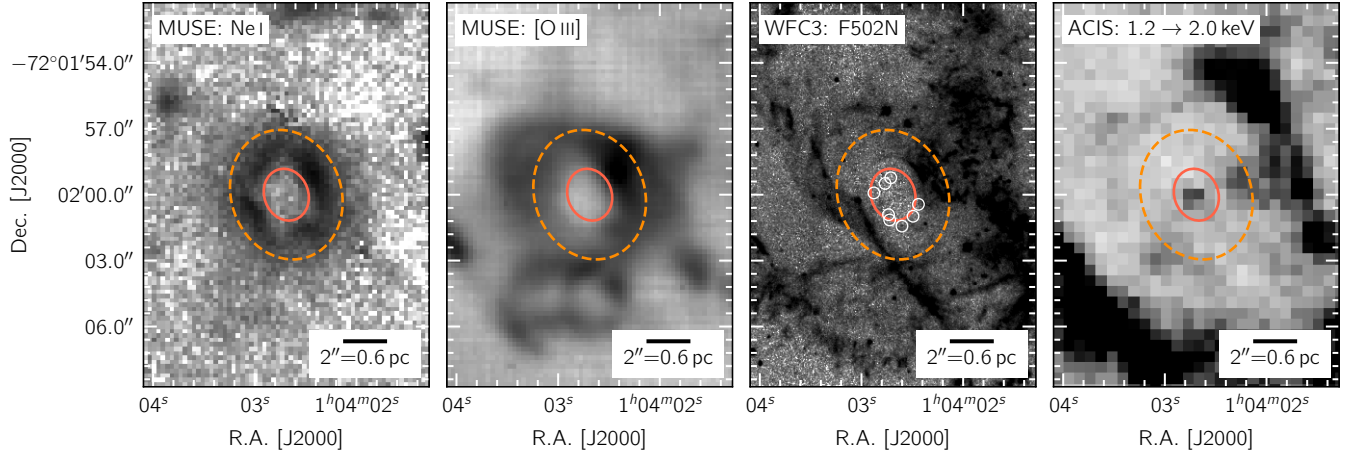
Figure 3: **Close-up view of the optical ring and CCO.** Left: Close-up, continuum-subtracted MUSE view of the optical low-ionization ring in the light of Ne I $\lambda6402$ (80 km s^{-1} bandpass). Middle-left: idem, in the light of [O III] $\lambda\lambda5007$ (80 km s^{-1} bandpass). A large ring-like structure is detected, despite the presence of some contaminating O-rich knots visible via their (redshifted) [O III] $\lambda4959$ emission. Middle-right: close-up *HST* ACS F475W view of the same area. The complex structures of the fast ejecta are readily visible. So is a smooth elliptical arc spatially coherent with the ring identified with MUSE. All confirmed optical point-sources in the vicinity of the torus center are marked with white circles. Right: *CXO* ACIS view of the same area in the 1.2–2.0 keV band, revealing the X-ray point source spatially coincident with the center of the optical gas ring revealed by MUSE. Two ellipses inclined at 20° East-of-North with an axis ratio of 1.2, semi-major axis of 1.2$''$ and 3.0$''$, and centered at R.A.: 01^{h}04^{m}02.^{s}7; Dec.: -72°02$'$00.$''$2 trace the inner and outer edge of the torus in all panels.

ciated with MUSE datacubes (Weilbacher et al. 2015; Vogt 2015).

The exact physical mechanism(s) responsible for the excitation of the low-ionization ring remains uncertain. Its optical spectrum and kinematics are consistent with dense, photoionized material which has not yet passed through the reverse shock. Quantifying the respective influence of photoionization by the CCO and/or by the overlying reverse shocked ejecta (for example, as modelled for SN 1006; Hamilton & Fesen 1988) will require theoretical modelling beyond the scope of this Letter.

The existence of a slowly expanding torus of low-ionization material surrounding the CCO of E 0102 leads us to propose this location as the actual supernova explosion site of the system. If ejected during the supernova explosion, the slowly expanding material in the torus (in sharp contrast with the large velocities measured elsewhere in E 0102) would have originated from close to the supernova mass cut: the surface separating ejected material from material that forms the CCO (Umeda & Yoshida 2016; Hix & Harris 2016). But we also note that our current kinematic measurements do not rule out the possibility that this structure could pre-date the supernova explosion by a few kyr. Either way, given that the CCO is still located within ~1.2$''$ from center of the optical ring 2050 yr after the supernova explosion, we can set an upper-limit on the transverse velocity of the CCO of $\lesssim$170 km s^{-1}. In this scenario, our newly defined explosion center would be located 5.9$''$($\equiv$1.77 pc) from

the explosion center derived from the fast ejecta proper motion (Fig.1 and Finkelstein et al. 2006) – well within the 2-σ(=6.8$''$) uncertainty associated with that measurement. Setting the explosion site of E 0102 at the current location of the CCO would however imply a large offset with respect to the rather regular outer envelope of the X-ray emission of this SNR, requiring a specific set of circumstances to shape the expansion of the forward shock wave into such a regular structure.

In the alternative scenario, the SN explosion occurred elsewhere, away from the current location of the CCO. Under these circumstances, we may be observing a CCO with high transverse velocity -e.g. ~850 km s^{-1} in the plane-of-the-sky assuming the explosion center from Finkelstein et al. (2006)- as it catches up and collides (possibly) with surrounding ejecta. But given the timescales involved, we fail, at this point in time, to identify a physical mechanism able to account for the dimensions and kinematics of the low-ionization ring under these circumstances. A re-analysis of existing archival *HST* observations of E 0102 spanning >8 yr should help refine the measurement of the explosion center from the kinematics of the fast ejecta in E 0102. If precise enough, such a refined measurement can provide a strong test of our presently favored scenario: that of the SN explosion originating at the current location of the CCO. At the same time, follow-up observations of the ring surrounding the CCO, with higher spatial resolution, are warranted to resolve the sub-structures within the ring, link the low-
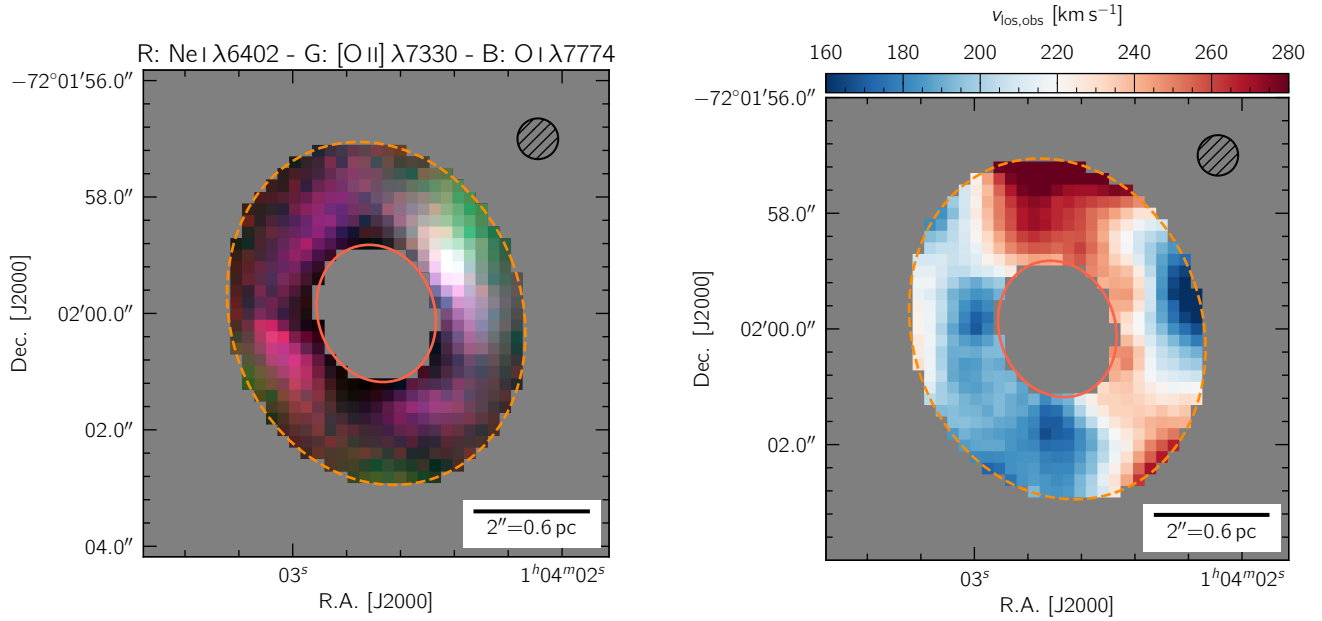
Figure 4: **Spectral analysis of the optical ring.** Left: pseudo-RGB image of the optical ring in the light of Ne I $\lambda6402$ (red channel), [O II] $\lambda7330$ (green channel) and O I $\lambda7774$ (blue channel). The low-ionization, denser material appears in pink. It is systematically located inwards of lower-density, higher-ionization material (in green). This image is reconstructed using the fitted line fluxes for each spaxel. The spatial resolution of the data (set by the seeing during the MUSE observations) is indicated by the dashed circle. The full and dashed ellipses trace the spatial extent of the optical ring, as indicated in Fig. 3. Right: observed LOS velocity of the gas, derived for each spaxel from their full spectral fit. The *blueshifted trough* to the West is present in a region of low surface brightness for the low-ionization lines, and the kinematic fit might be influenced by contaminating emission from fast ejecta in this area. Overall, the kinematic pattern is suggestive of an expanding torus, tilted with respect to the plane-of-the-sky. Small-scale variations should not be over-interpreted, given the spatial resolution of this dataset, and the typical MUSE kinematic fitting artefacts, visible to the trained eye as vertical and horizontal jumps (Weilbacher et al. 2015; Vogt 2015).

ionization material to the elliptical [O III] arc detected in *HST* images of the area, and refine the derivation of its kinematic signature and age. The Adaptive Optics modes of MUSE appear particularly suited to the task.

Online Content   Methods, along with any additional Extended Data display items and Source Data, are available in the online version of the paper; references unique to these sections appear only in the online paper.

References

Astropy Collaboration, Robitaille, T. P., Tollerud, E. J., et al. 2013, A&A, 558, A33

Bacon, R., Accardo, M., Adjali, L., et al. 2010, in Proc. SPIE, Vol. 7735, Ground-Based and Airborne Instrumentation for Astronomy III, 773508

Blair, W. P., Morse, J. A., Raymond, J. C., et al. 2000, ApJ, 537, 667

Bonnarel, F., Fernique, P., Bienaymé, O., et al. 2000, A&ASupplement Series, 143, 33

Camilo, F., Manchester, R. N., Gaensler, B. M., Lorimer, D. R., & Sarkissian, J. 2002, The ApJL, 567, L71

Chakrabarty, D., Pivovaroff, M. J., Hernquist, L. E., Heyl, J. S., & Narayan, R. 2001, ApJ, 548, 800

Cleveland, W. S. 1979, Journal of the American Statistical Association, 74, 829

Dickey, J. M. & Lockman, F. J. 1990, ARAA, 28, 215

Dopita, M. A., Tuohy, I. R., & Mathewson, D. S. 1981, The ApJL, 248, L105

Finkelstein, S. L., Morse, J. A., Green, J. C., et al. 2006, ApJ, 641, 919

Gaia Collaboration, Brown, A. G. A., Vallenari, A., et al. 2016a, A&A, 595, A2

Gaia Collaboration, Prusti, T., de Bruijne, J. H. J., et al. 2016b, A&A, 595, A1

Gilli, R., Comastri, A., & Hasinger, G. 2007, A&A, 463, 79

Graczyk, D., Pietrzyński, G., Thompson, I. B., et al. 2014, ApJ, 780, 59

Hamilton, A. J. S. & Fesen, R. A. 1988, ApJ, 327, 178

Helou, G., Madore, B. F., Schmitz, M., et al. 1991, Databases and On-line Data in Astronomy, 171, 89

Hix, W. R. & Harris, J. A. 2016, in Handbook of Supernovae, ed. A. W. Alsabti & P. Murdin (Springer International Publishing), 1–19

Hunter, J. D. 2007, Computing in Science and Engineering, 9, 90

Joye, W. A. & Mandel, E. 2003, in Astronomical Data Analysis Software and Systems XII ASP Conference Series, Vol. 295, 489

Kramida, A., Ralchenko, Y., Reader, J., & Team, N. A. 2016, NIST Atomic Spectra Database (Ver. 5.4)

Mereghetti, S., Tiengo, A., & Israel, G. L. 2002, ApJ, 569, 275

Middleditch, J. & Pennypacker, C. 1985, Nature, 313, 659

Mignani, R. P., de Luca, A., Mereghetti, S., & Caraveo, P. A. 2009, A&A, 500, 1211

Mignani, R. P., Sartori, A., de Luca, A., et al. 2010, A&A, 515, A110

Moré, J. J. 1978, in Numerical Analysis: Proceedings of the Biennial Conference Held at Dundee, June 28–July 1, 1977 (Springer Berlin Heidelberg), 105–116

Park, S., Hughes, J. P., Slane, P. O., et al. 2007, The ApJL, 670, L121

Pavlov, G. G. & Luna, G. J. M. 2009, ApJ, 703, 910

Pavlov, G. G., Sanwal, D., & Teter, M. A. 2004, in IAU Symposium, ed. F. Camilo & B. M. Gaensler, Vol. 218, eprint: arXiv:astro-ph/0311526, 239

Petre, R., Becker, C. M., & Winkler, P. F. 1996, The ApJL, 465, L43

Plucinsky, P. P., Beardmore, A. P., Foster, A., et al. 2017, A&A, 597, A35

Robitaille, T. & Bressert, E. 2012, Astrophysics Source Code Library, ascl:1208.017

Rutkowski, M. J., Schlegel, E. M., Keohane, J. W., & Windhorst, R. A. 2010, ApJ, 715, 908

Sasaki, M., Gaetz, T. J., Blair, W. P., et al. 2006, ApJ, 642, 260

Scowcroft, V., Freedman, W. L., Madore, B. F., et al. 2016, ApJ, 816, 49

Seabold, S. & Perktold, J. 2010, in Proc. of the 9th Python in Science Conference, 57–61

Seitenzahl, I. R., Vogt, F. P. A., Terry, J. P., et al. 2018, The ApJL, 853, L32

Seward, F. D., Harnden, Jr., F. R., & Helfand, D. J. 1984, The ApJL, 287, L19

Seward, F. D. & Mitchell, M. 1981, ApJ, 243, 736

Sutherland, R. S. & Dopita, M. A. 1995, ApJ, 439, 381

Umeda, H. & Yoshida, T. 2016, in Handbook of Supernovae, ed. A. W. Alsabti & P. Murdin (Springer International Publishing), 1–18

Viganò, D., Rea, N., Pons, J. A., et al. 2013, MNRAS, 434, 123

Vogt, F. P. A. 2015, PhD Thesis, Australian National University

Vogt, F. P. A., Seitenzahl, I. R., Dopita, M. A., & Ghavamian, P. 2017, A&A, 602, L4

Wang, Z., Kaplan, D. L., & Chakrabarty, D. 2007, ApJ, 655, 261

Weilbacher, P. M., Monreal-Ibero, A., Kollatschny, W., et al. 2015, A&A, 582, A114

Supplementary Information   is available in the online version of the paper.

Author Contributions

F.P.A.V. reduced and lead the analysis of the MUSE datacube. E.S.B. lead the spectral analysis of the Chandra dataset. All authors contributed to the interpretation of the observations, and the writing of the manuscript.

Author Information

The authors declare no competing financial interests. Readers are welcome to comment on the online version of the paper. Correspondence and requests for materials should be addressed to F.P.A.V (frederic.vogt@alumni.anu.edu.au).

Supplementary Information

Observations, data reduction & post-processing

MUSE The MUSE observations of E 0102 acquired under Director Discretionary Time program 297.D-5058 (P.I.: Vogt) are comprised of nine 900 s exposures on-source. The detailed observing strategy and data reduction procedures are described exhaustively in Vogt et al. (2017), to which we refer the interested reader for details. Similarly to that work, the combined MUSE cube discussed in the present report was continuum-subtracted using the Locally Weighted Scatterplot Smoothing algorithm (Cleveland 1979). This non-parametric approach is particularly suitable to reliably remove both the stellar and nebular continuum in all spaxels of the datacube without the need for manual interaction.

The one major difference between the MUSE datacube of E 0102 described in Vogt et al. (2017) and this work lies in the World Coordinate System (WCS) solution. For this analysis, we have refined the WCS solution (then derived by comparing the MUSE white-light image with the Digitized Sky Survey 2 red image of the area) by anchoring it to the *Gaia* (Gaia Collaboration et al. 2016b) Data Release 1 (DR1; Gaia Collaboration et al. 2016a) entries of the area. In doing so, we estimate our absolute WCS accuracy to be of the order of $0.2''$.

CXO E 0102 has been used as an X-ray calibration source for many years (Plucinsky et al. 2017), so that there exist numerous *CXO* observations of this system in the archive. When selecting datasets to assemble a deep X-ray view of E 0102, we applied the following, minimal selection criteria:

- DATAMODE = VFAINT

- no CC-mode observations

- $|\text{FP\_TEMP} - 153.3| < 2°$

- SEPN ≤ 1.2 arcmin, with the reference point set to R.A.:$01^h04^m02^s.4$, Dec.:-72°01'55''.3 [J2000].

These criteria ensure that we combine a uniform set of observations with minimal instrumental background. The last condition ensures that we use the observations with the highest possible spatial resolution, by using only those pointings with E 0102 close from the optical axis of the telescope. The resulting list of 28 observations matching these criteria is presented in Table 1. We did not apply any selection criteria on the year or the depth of the observations: a direct consequence of setting the focus of our analysis on the characterization of the detected X-ray point source (for which we find no evidence of proper motion in the *CXO* observations), rather than on the fast moving ejecta.

We fetched and reprocessed all these datasets using CIAO 4.9 and CALDB 4.7.3, via the CHANDRA_REPRO routine. We

Table 1: List of *CXO* observations of E 0102 reprocessed for this work. All these datasets but three (subject to flaring) were combined and analyzed jointly.

Obs. I.D.	Date	Depth [ks]	Signs of flaring ?
3519	2003-02-01	8.0	
3520	2003-02-01	7.6	
3545	2003-08-08	7.9	
3544	2003-08-10	7.9	
5123	2003-12-15	20.3	yes
5124	2003-12-15	7.9	yes
5131	2004-04-05	8.0	
5130	2004-04-09	19.4	
6075	2004-12-18	7.9	
6042	2005-04-12	18.9	
6043	2005-04-18	7.9	
6074	2004-12-16	19.8	yes
6758	2006-03-19	8.1	
6765	2006-03-19	7.6	
6759	2006-03-21	17.9	
6766	2006-06-06	19.7	
8365	2007-02-11	21.0	
9694	2008-02-07	19.2	
10654	2009-03-01	7.3	
10655	2009-03-01	6.8	
10656	2009-03-06	7.8	
11957	2009-12-30	18.4	
13093	2011-02-01	19.0	
14258	2012-01-12	19.0	
15467	2013-01-28	19.1	
16589	2014-03-27	9.6	
18418	2016-03-15	14.3	
19850	2017-03-19	14.3	

searched for evidence of background flares by generating images in the 0.5-8.0 keV energy range while removing the bright sources in the field of view, including E 0102. Light curves were then created from the entire remaining image and inspected by eye. We dropped three observations (Obs. I.D.: 5123, 5124 and 6074) that show signs of flaring, prior to combining the remaining ones using the REPROJECT_OBS routine. All X-ray images of E 0102 presented in this work were extracted from this combined, reprojected dataset. We did not perform any adjustment to the existing WCS solution of the combined dataset, which given our *target on-axis* selection criteria can be expected to be of the order of 0.6″.

HST We downloaded from the Barbara A. Mikulski Archive for the Space Telescopes (MAST) all the observations of E 0102 acquired with the Advanced Camera for Survey (ACS) and the Wide Field Camera 3 (WFC3) that used narrow, medium and wide filters. These belong to three observing programs: 12001 (ACS, P.I.: Green), 12858 (ACS, P.I.: Madore) and 13378 (WFC3, P.I.: Milisavljevic). The exhaustive list of all the individual observations is presented in Table 2.

All the calibrated, CTE-corrected, individual exposures (*_FLC.FITS) obtained from MAST were fed to the TWEAKREG routine to correct their WCS solutions. We used a custom PYTHON script relying on the DRIZZLEPAC 2.1.13, ASTROQUERY and ASTROPY packages to do so automatically for all the filters. We used the *Gaia* (Gaia Collaboration et al. 2016b) DR1 (Gaia Collaboration et al. 2016a) catalogue as the reference set of point source coordinates and fluxes. Using the same script, we subsequently fed all the images for a given filter to the ASTRODRIZZLE routine, and combined them into a single final frame. We set the pixel scale to 0.04″ for all filters for simplicity, but note that this value does not affect significantly our conclusions. We also note that combining observations separated by several years is not ideal from the perspective of the fast ejecta (whose proper motion imply a blurring of the final image). It is however a suitable approach in the present case, i.e. in order to look for an optical counterpart to the X-ray point source detected with *CXO*, provided that its proper motion is smaller than ∼0.08/10=0.008″ yr^{-1}≅2350 km s^{-1}.

Postage stamp images of the optical ring area detected with MUSE, for all re-processed *HST* camera+filter combinations, are presented in Fig. 5. We find no evidence for an optical counterpart to the X-ray point source detected with *CXO*. Four point sources are detected within the central gap of the low-ionization optical ring detected with MUSE, but we rule them out as suitable candidate based on their largely off-center locations. E 0102 was not observed by *HST* down to the same depth in each filter. The strongest constraints for the brightness of a possible optical counterpart come from the ACS F475W image (4324 s on-source), the ACS F775W image (2160 s on-source), and the ACS F850LP (2160 s on-source). Specifically, we derive an upper

limit for the magnitude of a possible optical counterpart to the X-ray source of $m_{\mathrm{F475W}} > 23.0$, $m_{\mathrm{F775W}} > 24.5$ and $m_{\mathrm{F850LP}} > 25.0$, noting that the F475W image is severely affected by contaminating [O III] λλ4959,5007 emission from the fast ejecta, falling within the filter bandpass.

CXO characterization of the CCO in E 0102

Spatial characterization Combined X-ray images of E 0102 were created in the standard *CXO* ACIS source detection energy bands, as well as the ultrasoft band (0.2–0.5 keV), using the CIAO script MERGE_OBS. We ran the Mexican-Hat wavelet source detection tool WAVDETECT on all the combined images, which confirmed the presence of the point source *p1* already detected by Rutkowski et al. (2010), and coincident with the low-ionization optical ring discovered with MUSE. As we are exclusively searching for a point source embedded in the diffuse emission of the hot ejecta from the SNR, the source detection algorithm was run with no point spread function (PSF) map on "fine" scales (the WAVDETECT scales parameter was set to "1 2"). The derived spatial parameters for each band are summarized in Table 3.

Without a PSF map, WAVDETECT uses the smallest wavelet scale found to derive the source properties. This approach may lead to incorrect parameters at large off-axis angles, but our *target on-axis* selection criteria for the *CXO* datasets ensures that this will not have a very significant effect in the present case. The detection process itself is unaffected by the lack of inclusion of a PSF map. We did experiment with PSF maps weighted by both exposure time and exposure map for the combined broad band dataset. But in each instance, the algorithm detects the entire filamentary structure of E 0102, rather than a point source itself[2].

Spectral characterization We manually extracted the counts of the source *p1* in all bands using the region derived from the automated point source search in the medium *CXO* band, where it is most reliably detected by WAVDETECT (see Table 3). Background counts are derived from an annulus centered on the source, and with inner and outer radii of 1.2″ and 1.8″, respectively. The counts derived from each band are summarized in Table 4.

Our chosen parameters for the "background annulus" are motivated by the complex X-ray background emission throughout E 0102. This annulus is narrow enough to avoid brighter filamentary structures nearby, but large enough for a reliable estimate of the local background level close to and around the source. Whilst our region size is small, approximately 90% of the encircled energy still lies within 1″ of the central pixel[3]. For example, Pavlov & Luna (2009)

---

[2]For more details on running WAVDETECT on combined datasets, see *http://cxc.harvard.edu/ciao/threads/wavdetect merged/index.html*

[3]see Figure 6.10, in *http://cxc.cfa.harvard.edu/proposer/POG/html/ACIS.html*

Table 2: List of *HST* observations of E 0102 reprocessed for this work.

Program I.D.	Observation I.D.	P.I.	Observation Date	Instrument	Filter	Exposure time [s]
13378	ICBQ01010	Milisavljevic	2014-05-12	WFC3/UVIS	F280N	1650
13378	ICBQ01020	Milisavljevic	2014-05-12	WFC3/UVIS	F280N	1100
13378	ICBQ01050	Milisavljevic	2014-05-12	WFC3/UVIS	F373N	2268
13378	ICBQ03070	Milisavljevic	2014-05-14	WFC3/UVIS	F467M	1362
12001	J8R802010	Green	2003-10-15	ACS/WFC	F475W	1520
12001	J8R802011	Green	2003-10-15	ACS/WFC	F475W	760
12858	JBXR02010	Madore	2013-04-10	ACS/WFC	F475W	2044
13378	ICBQ02010	Milisavljevic	2014-05-13	WFC3/UVIS	F502N	1653
13378	ICBQ02020	Milisavljevic	2014-05-13	WFC3/UVIS	F502N	1100
12001	J8R802020	Green	2003-10-15	ACS/WFC	F550M	1800
12001	J8R802021	Green	2003-10-15	ACS/WFC	F550M	900
13378	ICBQ03080	Milisavljevic	2014-05-14	WFC3/UVIS	F645N	1350
13378	ICBQ03010	Milisavljevic	2014-05-14	WFC3/UVIS	F657N	1653
13378	ICBQ03020	Milisavljevic	2014-05-14	WFC3/UVIS	F657N	1102
12001	J8R802030	Green	2003-10-15	ACS/WFC	F658N	1440
12001	J8R802031	Green	2003-10-15	ACS/WFC	F658N	720
13378	ICBQ03030	Milisavljevic	2014-05-14	WFC3/UVIS	F665N	1719
13378	ICBQ03040	Milisavljevic	2014-05-14	WFC3/UVIS	F665N	1146
13378	ICBQ03050	Milisavljevic	2014-05-14	WFC3/UVIS	F673N	1719
13378	ICBQ03060	Milisavljevic	2014-05-14	WFC3/UVIS	F673N	1146
12001	J8R802050	Green	2003-10-15	ACS/WFC	F775W	1440
12001	J8R802051	Green	2003-10-15	ACS/WFC	F775W	720
12001	J8R802040	Green	2003-10-15	ACS/WFC	F850LP	1440
12001	J8R802041	Green	2003-10-15	ACS/WFC	F850LP	720

Table 3: Spatial characterization of the point source *p1* detected in E 0102 by *CXO*, derived from wavdetect.

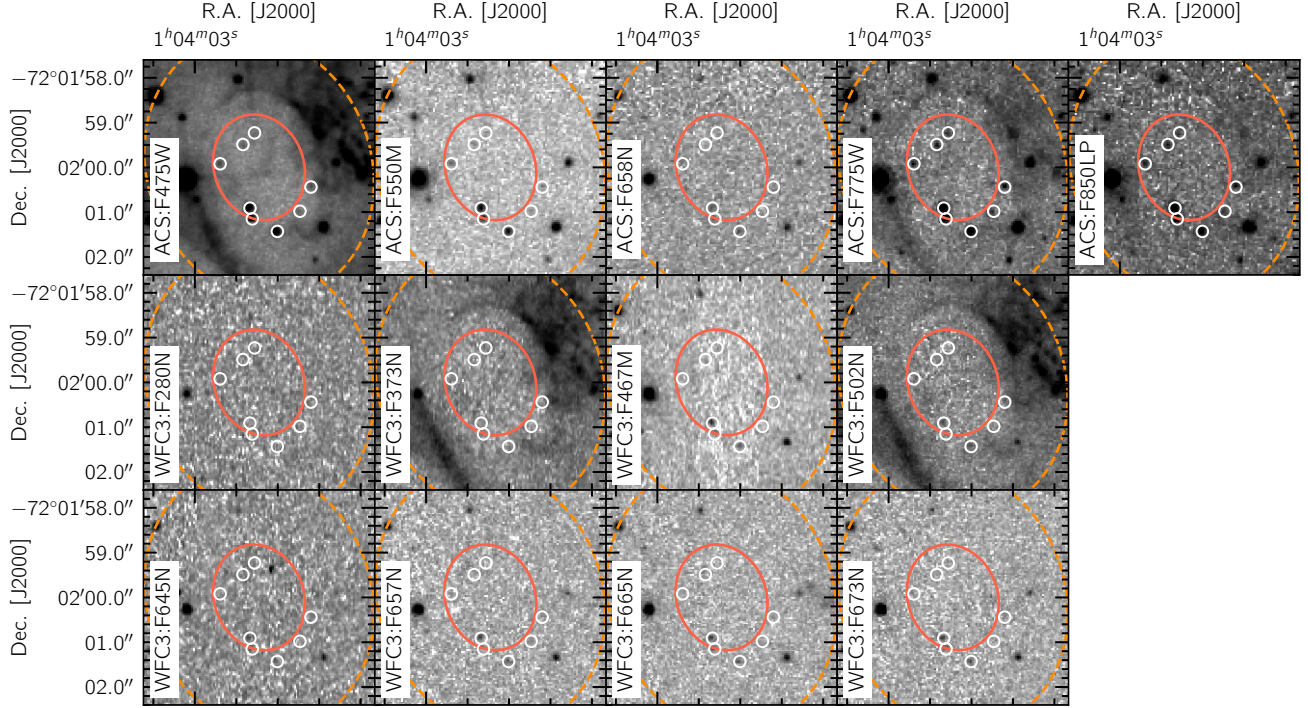| Band	Energy [keV]	R.A. [J2000]	Dec. [J2000]	Semi-major axis [arcsec]	Semi-minor axis [arcsec]	Pos. Angle [deg]	Detection significance
Broad	0.5–7.0	01:04:02.73	-72:02:00.36	1.6	1.1	50.9	8.60
Ultrasoft	0.2–0.5	01:04:02.73	-72:02:00.23	1.2	1.0	58.5	2.10
Soft	0.5–1.2	01:04:02.77	-72:02:00.66	1.9	0.9	74.2	5.78
Medium	1.2–2.0	01:04:02.75	-72:02:00.14	1.2	1.0	54.0	8.30
Hard	2.0–7.0	01:04:02.75	-72:02:00.19	2.2	1.8	91.8	5.45

Figure 5: **Detailed view of the torus region in archival *HST* ACS and WFC3 observations.** The spatial extent of the optical ring detected with MUSE is traced using the ellipses introduced in Fig. 3. Point-sources detected near/within the inner ellipse (in at least one image) are marked with white circles. We find no candidate near the center of the ring. The presence of the filamentary structure of ejecta is visible in the F475W (via [O III] $\lambda\lambda$4959,5007), F775W (via O I λ7774), F850LP (via O I $\lambda\lambda$9262,9266), F373N (via [O II] $\lambda\lambda$3726,3728) and F502N (via [O III] $\lambda\lambda$4959,5007) images.

also adopt a similar region size (1.5″ in radius) in their analysis of the Galactic CCO in Cas A.

The low counts associated with source *p1* hinder our ability to extract robust parameters from a direct spectral fitting. Instead, for comparison purposes, we first investigate how the CCO of Cas A would appear to an observer if it were located at the distance of the SMC, with an absorbing column equal to that of 1E0102. We simulate the double-blackbody model of Pavlov & Luna (2009) to do so, using XSPEC v.12.9.0 and the FAKEIT command. These authors fit absorbed blackbody, power law and neutron star atmosphere models to a single 70.2 ks *CXO* observation of Cas A, with a count rate of 0.1 counts s^{-1}. They find that the X-ray spectrum of the CCO of Cas A is equally well described by both an absorbed double neutron star model (represented as $wabs \times (nsa + nsa)$ in XSPEC) and an absorbed double blackbody model (represented as $wabs \times (bbody + bbody)$ in XSPEC).

We include two absorption terms to the model: one to account for the Galactic absorption (set to 5.36×10^{20} cm^{-2} Dickey & Lockman 1990), and another set to the intrinsic absorption in the south-east region of 1E0102, where the source *p1* is located (4×10^{20} cm^{-2} Sasaki et al. 2006). The spectrum is then normalised to have the same unabsorbed

luminosity as that reported by Pavlov & Luna (2009), over the same energy range. In summary, our final model is represented by $C \times wabs_{Gal} \times wabs_i \times (bbody + bbody)$ in XSPEC, where C is a constant. We simulate the spectrum of such a source using the *CXO* cycle 19 canned response matrices[4] and an exposure time of 323 ks, matching the total depth of our combined *CXO* observations.

We compare the simulated spectrum of Cas A with the measured counts of the source *p1* (in each of the narrow energy bands) in Fig. 2: *p1* appears cooler than would a Cas A-like CCO at the same location. This is not necessarily surprising, given that E 0102 is ∼1700 yr older than Cas A.

Next, to derive X-ray fluxes and luminosities for the source *p1* in E 0102, we use XSPEC's FAKEIT with the cycle 19 canned response matrices to simulate absorbed single blackbody models in the same manner as above. These models are represented by $C \times wabs_{Gal} \times wabs_i \times bbody$ in XSPEC. We restrict ourselves to single blackbody models, as the counts associated with the source *p1* are insufficient to reliably constraint more complex ones, including double blackbody models. The Galactic and intrinsic absorption components are once again set to 5.36×10^{20} cm^{-2}

---

[4]available at *http://cxc.harvard.edu/caldb/prop_plan/imaging/index.html*

Table 4:   X-ray properties of the point source *p1*, derived from our best-fit, absorbed, single blackbody model with $kT_{BB} = 0.19$ keV.

Band	Energy [keV]	Counts$_{\text{observed}}$[a]	Counts$_{\text{simulated}}$[b]	$F_{-14, \text{ model}}$[c] [erg cm^{-2} s^{-1}]	$F_{-14, \text{ data}}$[d] [erg cm^{-2} s^{-1}]	$L_{i,33,\text{model}}$[e] [erg s^{-1}]
Broad	0.5–7.0	469 ± 56	469	1.37	1.4 ± 0.2	9.0 ± 1.3
Ultrasoft	0.2–0.5	< 40[f]	4	0.17	< 2.1[f]	3.2 ± 0.4
Soft	0.5–1.2	287 ± 51	279	1.11	1.1 ± 0.2	7.5 ± 1.1
Medium	1.2–2.0	143 ± 22	172	0.28	0.24 ± 0.04	1.4 ± 0.2
Hard	2.0–7.0	39 ± 9	7	0.02	0.10 ± 0.02	0.08 ± 0.01

[a] Observed (background subtracted) counts for the source *p1*.
[b] Simulated source counts for the best-fit, absorbed single blackbody model (*wabs* × *wabs* × *bbody*, with $kT_{BB} = 0.19$ keV).
[c] The X-ray flux (in units of 10^{-14} erg cm^{-2} s^{-1}) of the best-fit, absorbed single blackbody model.
[d] The observed X-ray flux (in units of 10^{-14} erg cm^{-2} s^{-1}) of the source *p1*, computed with the ECFs derived (for each energy band) from the best-fit, absorbed single blackbody model and associated simulated dataset.
[e] Intrinsic (i.e. unabsorbed) X-ray luminosity implied from the assumed absorbed Blackbody model, assuming a distance of 62.1 kpc to the SMC and a 10% error on the exact distance to E 0102 within the SMC.
[f] 3σ upper limit.

and 4×10^{20} cm^{-2}, respectively. We generate spectra with temperatures kT_{BB} ranging from 0.10–0.49 keV in steps of 0.01 keV. Each spectrum is normalised so that the total number of counts over 0.5–7.0 keV (i.e. the broad band) in a 323 ks exposure is consistent with that of the source *p1* detected in our merged data set of E 0102. From these simulated spectra, we obtain the count rates, absorbed fluxes, and intrinsic luminosities in each of the *CXO* narrow bands. All our models are compared with the measured counts of the source *p1* in Figs 6 and 7.

We calculate the χ^2 of each of the single blackbody models with respect to the data over both the 0.5–7.0 keV and 0.2–7.0 keV energy ranges. We exclude the ultrasoft band from the first range, as the *CXO* response files are less accurate below 0.5 keV[5]. We show in Fig. 8 the distribution of these χ^2 values as a function of the blackbody temperature of the models, together with the fourth order polynomial best fit to the 0.5–0.7 keV data. We find that the source *p1* is best characterised by an absorbed blackbody with kT_{BB} 0.19 ± 0.02 keV.

Fitting a single blackbody model to Cas A (with a derived a temperature of 0.4 keV) underestimates the CCO flux at higher energies (Pavlov & Luna 2009). The same can be seen in our simulations: our best-fit, absorbed single blackbody model underestimate the number counts of the source *p1* in the hard *CXO* band. The flux values associated with the best-fit $kT_{BB} = 0.19$ keV model are included in Table 4 along with the implied intrinsic (i.e. un-absorbed) X-ray luminosity. The errors associated with the latter stem

---
[5] see *http://cxc.harvard.edu/caldb/prop_plan/imaging/index.html*

from an assumed 10% uncertainty in the depth of E 0102 within the SMC. In the same Table, we also present the observed X-ray flux of the source *p1*, computed from the observed data using the energy conversion factors (ECFs) derived (for each energy band) from the best-fit, absorbed single blackbody model with $kT_{BB} = 0.19$ keV.

We note that our derived fluxes and luminosities are subject to caveats. First, our simulated spectra assume that we have a single 323 ks observation performed in cycle 19 of *CXO*'s lifetime, rather than several observations spanning over a decade. Second, the background subtraction and determination for the point source *p1* is non-trival, as it is embedded in bright, spatially complex background emission. A more complex spectroscopic analysis of this X-ray point source, outside the scope of this report, ought to address these points carefully.

MUSE spectral characterization of the optical ring

We performed a full fit of the MUSE spectra associated with each of the 492 spaxels contained within the area of the optical ring. The fitted spaxels are located within two ellipses with semi-major axis of 1.2″ and 3.0″ centered on the CCO (R.A: $01^h04^m02.7^s$ — Dec: -72°02′00.2″ [J2000]), and rotated by 20° East-of-North. The ring is detected in 35 lines of Ne I, O I, [O I], and [C I], all of which were identified following a manual, visual inspection of every spectral channel in the continuum-subtracted MUSE datacube (see Fig. 9). An intensity drop spatially coincident with the ring is also detected in 4 lines of [O III] and [O II], but the surrounding

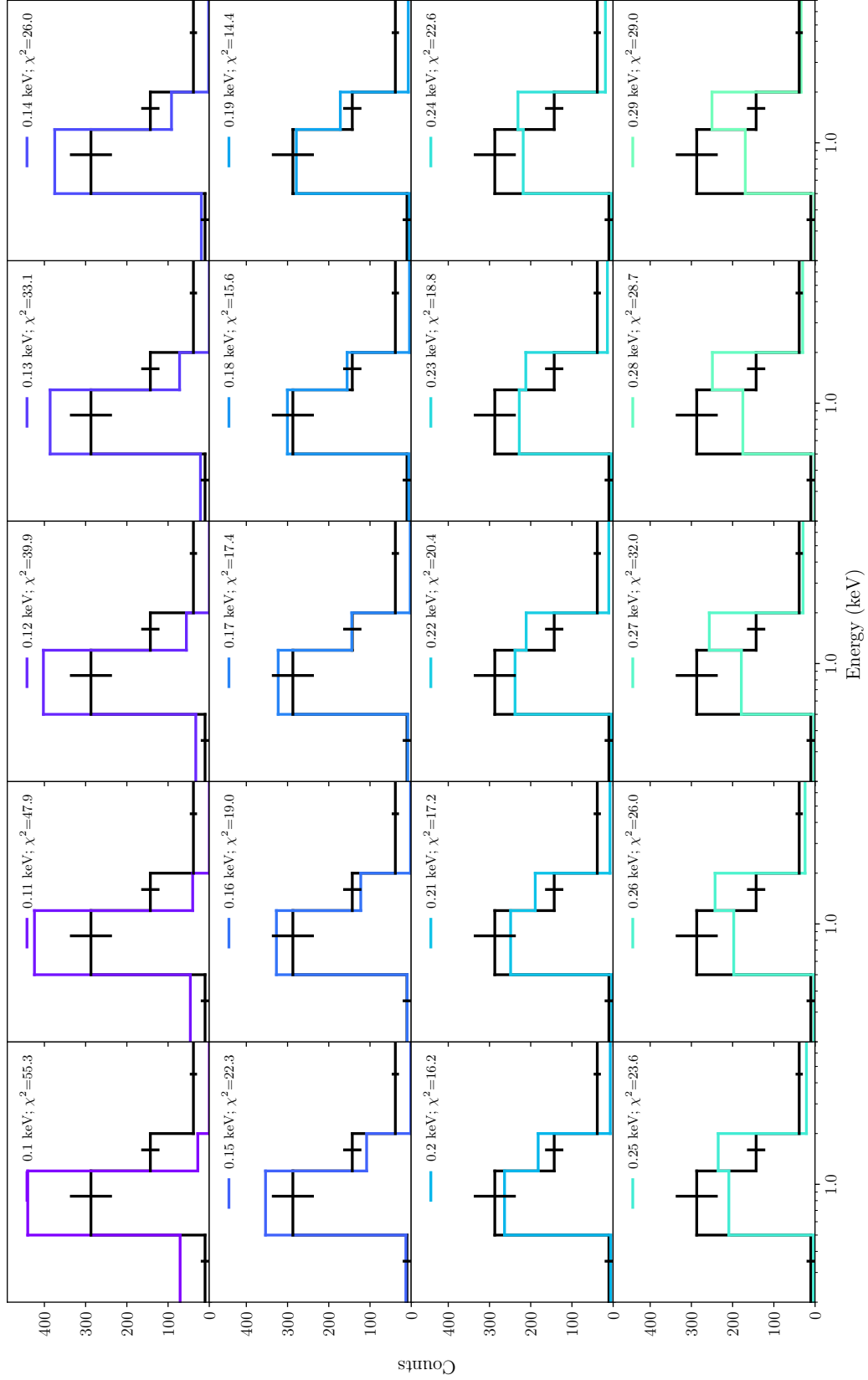Figure 6: Energy distribution of the X-ray point source *p1* (black curves), compared with absorbed, single blackbody models (colored curves) with kT_{BB} ranging from 0.10–0.29 keV in steps of 0.01 keV. The χ^2 of the fit, computed over the 0.5–0.7 keV energy range, is shown in each panel.
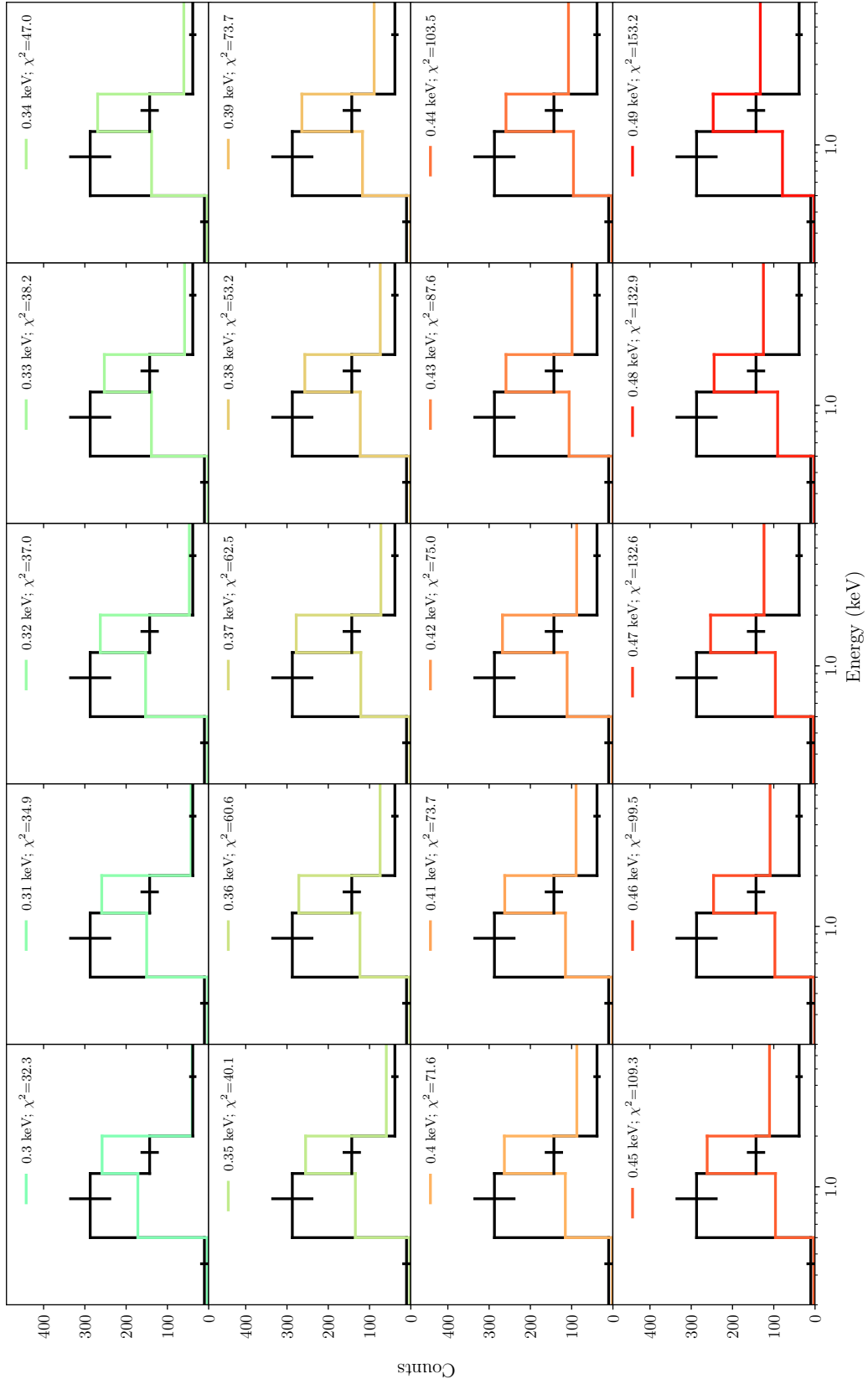
Figure 7: Same as Fig. 6, but for models with kT_{BB} ranging from 0.30–0.49 keV.
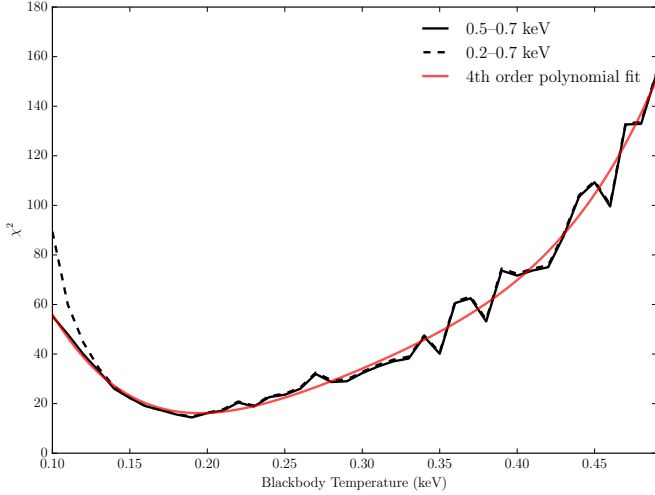
Figure 8: The χ^2 values for each single blackbody model fitted to the energy distribution of the point source *p1*, shown as a function of the model temperature and computed over the 0.5–0.7 keV (full black line) and 0.2–0.7 keV (dashed black line) energy range. The best-fit fourth-order polynomial to the 0.5–0.7 keV dataset is shown with a red line.

emission of these lines is spatially more extended in comparison to the lower-ionization lines, as illustrated in Fig. 3. The low- and high-ionization lines thus likely originate from physically distinct volumes.

The line fitting is performed using a custom routine relying on the PYTHON implementation of MPFIT, a script that uses the Levenberg-Marquardt technique (Moré 1978) to solve least-squares problems, based on an original Fortran code part of the MINPACK-1 package. We do not include the [O III] $\lambda\lambda$4959,5007 lines in the fitting: their large intensity with respect to the lower-ionization emission lines and the presence of several fast ejecta knots throughout the footprint of the ring affect the derived kinematic signature of the ring. We do however include the [O II] $\lambda\lambda$7320,7330 lines in the list of fitted lines for comparison purposes, after having ensured that their inclusion does not affect the outcome of the spectral fit at a significant level. Finally, we do not include the Ne I λ6266, Ne I λ6334, Ne I λ6383, Ne I λ6678, Ne I λ6717, and Ne I λ8654 emission lines in the fit, as these lines are strongly contaminated by residual sky lines, bright emission lines from fast ejecta along specific lines-of-sight, and/or background H II-like emission.

For each of the 492 spaxels within the footprint of the ring, the selected 31 emission lines are fitted simultaneously, each with a single Gaussian component tied to a common, observed LOS velocity $v_{\text{los,obs}}$. The velocity dispersion $\sigma(\lambda)$ for a specific line wavelength λ is set to:

$$\sigma(\lambda) = \sqrt{\sigma_{\text{obs}}^2 + \sigma_{\text{inst}}(\lambda)^2}, \qquad (2)$$

with $\sigma_{\text{obs}} = 65$ km s^{-1} the assumed-constant underlying

gas velocity dispersion, and $\sigma_{\text{inst}}(\lambda)$ the wavelength-dependant instrumental spectral dispersion of MUSE. The ring emission lines are essential (spectrally) unresolved by MUSE. We here fix their underlying velocity dispersion to ensure a robust fit for all spaxels, including those towards the inner and outer edges of the ring with lower S/N, noting that the fitting results are not significantly affected by the exact value of σ_{obs}. Dedicated observations with higher spectral resolution are required to constrain this parameter.

The measured line fluxes for all fitted lines are presented in Table 5. The rest frame line wavelengths were obtained from the NIST Atomic Spectra Database (Kramida et al. 2016). The LOS velocity map of the ring is shown in Fig. 4, together with a pseudo-RGB image of the fitted area in the light of Ne I λ6402, [O II] λ7330, and O I λ7774. The mean fitted ring spectrum is compared to the observed spectra in Fig. 9. The mean velocity of the optical ring is (55 ± 10) km s^{-1} with respect to the background H II-like emission of the SMC. The uncertainty is dominated by the somewhat irregular appearance of the velocity map: the error associated with the fitting alone is of the order of 5 km s^{-1}.

15

Table 5: Total line fluxes $F_{\lambda,tot}$, average line flux surface densities $< F_\lambda >$, and associated 1-σ standard deviation $\sigma(F_\lambda)$ of the optical ring surrounding the CCO in E 0102. The exhaustive list of ring emission lines were identified by a visual, manual inspection of each spectral channel of the MUSE datacube. The line fluxes are derived from a simultaneous spectral fit on a spaxel-by-spaxel basis, for each of the 492 MUSE spaxels within the 19.7 square arcsec footprint of the ring.

Line	λ_{rest} [Å]	$F_{\lambda,tot}$ [10^{-18} erg s^{-1} cm^{-2}]	$< F_\lambda >$ [10^{-20} erg s^{-1} cm^{-2} arcsec^{-2}]	$\sigma(F_\lambda)$ [10^{-20} erg s^{-1} cm^{-2} arcsec^{-2}]
[O III]	4958.911	N/A	N/A	N/A
[O III]	5006.843	N/A	N/A	N/A
Ne I	5330.7775	136.6 ± 2.3	694.2 ± 11.9	460.4
O I	5435.78	39.7 ± 1.8	202.0 ± 9.0	236.4
Ne I	5852.4878	38.1 ± 1.7	193.5 ± 8.5	213.6
Ne I	5944.8340	49.1 ± 1.9	249.7 ± 9.5	249.3
Ne I	6074.3376	60.5 ± 1.7	307.3 ± 8.6	263.6
Ne I	6096.1630	70.7 ± 1.8	359.4 ± 9.1	286.9
Ne I	6143.0627	166.2 ± 1.9	844.7 ± 9.8	546.8
O I	6158.18	398.5 ± 2.0	2024.7 ± 10.3	886.9
Ne I	6266.4952	N/A	N/A	N/A
[O I]	6300.304	1799.1 ± 3.1	9142.0 ± 15.7	5858.3
Ne I	6334.4276	N/A	N/A	N/A
[O I]	6363.776	566.2 ± 2.1	2877.3 ± 10.6	1943.9
Ne I	6382.9914	N/A	N/A	N/A
Ne I	6402.248	373.6 ± 1.9	198.3 ± 9.6	736.4
O I	6454.44	78.6 ± 1.7	399.2 ± 8.5	303.4
Ne I	6506.5277	219.2 ± 1.7	1113.6 ± 8.9	561.7
Ne I	6532.8824	29.0 ± 1.3	147.6 ± 6.5	170.8
Ne I	6598.9528	34.3 ± 1.5	174.4 ± 7.7	184.2
Ne I	6678.2766	N/A	N/A	N/A
Ne I	6717.0430	N/A	N/A	N/A
Ne I	6929.4672	101.6 ± 1.4	516.3 ± 7.1	289.4
O I	7002.23	73.6 ± 1.3	374.2 ± 6.8	301.6
Ne I	7032.4128	113.5 ± 1.4	576.9 ± 6.9	303.8
Ne I	7245.1665	30.3 ± 1.5	153.7 ± 7.4	189.7
[O II]	7319.92	2357.5 ± 2.4	11979.1 ± 12.1	7512.0
[O II]	7330.19	1904.3 ± 2.2	9676.5 ± 11.1	5273.2
Ne I	7488.8712	43.3 ± 1.4	220.1 ± 7.0	181.5
Ne I	7535.7739	41.1 ± 1.3	208.8 ± 6.8	179.8
O I	7774.17	4442.1 ± 3.5	22571.6 ± 17.6	9614.1
Ne I	8377.6070	147.0 ± 2.3	747.0 ± 11.7	469.5
O I	8446.36	1419.1 ± 3.3	7210.8 ± 16.7	3949.6
Ne I	8495.3591	36.7 ± 1.7	186.6 ± 8.5	227.9
Ne I	8654.3828	N/A	N/A	N/A
[C I]	8727.13	44.9 ± 1.2	228.4 ± 6.3	211.1
Ne I	8780.6223	49.8 ± 1.6	252.9 ± 8.2	259.2
O I	9262.67	1246.7 ± 3.7	6334.7 ± 18.7	2758.9
O I	9266.01	1338.7 ± 3.7	6802.4 ± 18.9	3285.6

Figure 9: MUSE spectra for all 492 spaxels within the footprint of the low-ionization ring, shown as individual black lines with 5% transparency. Light-grey spectral regions indicate spatially-varying emission lines, associated with reverse-shocked fast ejecta (the most prominent example of which is associated with [O III] $\lambda\lambda$4959,5007). Darker, sharper emission lines are associated with the torus (and labelled using red dashed lines) or with background H II-like emission from the SMC (the most prominent examples of which are labelled using dot-dashed purple lines). Any other spectral feature is caused by the imperfect sky subtraction of the data (either for sky emission lines or telluric lines).